Photocatalysis
https://www.sciltp.com/journals/photocatalysis

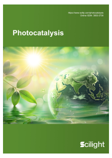

Article

Enhanced Hydrogen Production by Photoreforming on C_3N_4 Adjusting Exfoliation and Platinum Co-Catalyst Dispersity

Laura C. Valencia-Valero [1], Habiba Khiar [2,3], Noureddine Barka [2], Marta Giamberini [1] and Alberto Puga [1,*]

[1] Department of Chemical Engineering, Rovira i Virgili University, Av. Països Catalans, 43007 Tarragona, Spain
[2] Multidisciplinary Research and Innovation Laboratory, FP Khouribga, Sultan Moulay Slimane University of Beni Mellal, BP. 145, Khouribga 25000, Morocco
[3] LASIRE—Laboratory of Advanced Spectroscopy for Interactions, Reactivity and Environment, CNRS UMR 8516, Faculté de Sciences et Technologies, Université de Lille, 59655 Lille, France
* Correspondence: alberto.puga@urv.cat

How To Cite: Valencia-Valero, L.C.; Khiar, H.; Barka, N.; et al. Enhanced Hydrogen Production by Photoreforming on C_3N_4 Adjusting Exfoliation and Platinum Co-Catalyst Dispersity. *Photocatalysis* **2026**, *2*(2), 6. https://doi.org/10.53941/photocatalysis.2026.100006

Received: 20 April 2026
Revised: 5 June 2026
Accepted: 12 June 2026
Published: 29 June 2026

Abstract: This article explores the optimization of C_3N_4 photocatalyst synthesis using different precursors such as melamine, urea, and dicyandiamide, evaluating the resulting morphology, structure and properties, aiming at improved hydrogen evolution by photoreforming of oxygenated substrates. Exfoliation methods, chiefly thermal annealing and ultrasonication coupled to fractionation, were explored to obtain thin nanosheets of high surface area. Adjustment of platinum co-catalyst photodeposition was performed to optimise Pt nanoparticle loading and maximise their dispersity on C_3N_4 nanosheets, resulting in enhanced photocatalytic efficiency. Hydrogen production activity from model oxygenated substances of increasing structural complexity that could be representative of wastewater components, such as methanol, glycerol, glucose or poly(ethylene glycol), was evaluated. This systematic study allows to gain insight into the relationship between photocatalytic hydrogen evolution and the composition of residual aqueous effluents.

Keywords: carbon nitride; photoreforming; hydrogen; pollutants; waste; polymers

1. Introduction

The growing demand for clean energy has driven the exploration of innovative materials for photocatalytic hydrogen production [1]. Among these, graphitic carbon nitride (C_3N_4) stands out due to its two-dimensional structure based on repeating tri-s-triazine (heptazine) units interconnected by nitrogen bridges (Figure 1); this unique configuration, similar to graphene but with an appropriate bandgap (≈2.7 eV), enables efficient visible light absorption [2]. As a metal-free semiconductor, C_3N_4 avoids common drawbacks of metal-based photocatalysts, mainly reliance on critical raw materials or photocorrosion, while its π-conjugated system promotes electron delocalization for enhanced charge mobility [3–6]. However, rapid electron-hole recombination remains a key challenge, motivating strategies like heteroatom doping and heterojunction engineering to optimize its photophysical properties and light response [3,4].

Graphitic carbon nitride exhibits unique photoelectronic properties determined by the energy positions of its valence and conduction bands, which are equivalent to its highest occupied and lowest unoccupied molecular orbitals (HOMO and LUMO, respectively). Density functional theory calculations revealed that the HOMO primarily consists of nitrogen 2p orbitals, while the LUMO originates from carbon 2p orbitals [5,7]. This energetic configuration endows C_3N_4 with: (*i*) the ability to generate electron-hole pairs under visible light ($\lambda \leq 460$ nm); (*ii*) a sufficiently negative reduction potential (−1.3 eV) to reduce protons to H_2 ($E° = 0.00$ V vs. the normal hydrogen electrode, NHE) [8]; and (*iii*) an adequate oxidation potential (+1.4 eV) to degrade organic pollutants through reactive oxygen species (ROS, $E°(OH^•/OH^−) = 2.8$ V vs. NHE) [9]. These semiconductor properties are the basis of the photocatalytic activity of C_3N_4 in environmental remediation applications, chiefly pollutant degradation [9]. Under visible light, C_3N_4 effectively breaks down dyes [10], pharmaceuticals [11] or endocrine disruptors (e.g., bisphenol A) [12] via ROS-mediated oxidation. Beyond oxidation, C_3N_4 attracts greater interest due to its reductive photocatalytic properties leading to the generation of energy carriers, such as hydrogen.

Carbon nitride materials are typically synthesized by thermal polycondensation of appropriate nitrogen-rich precursors such as cyanamide [2], melamine [13–15], urea [16–18] or dicyandiamide [19] at 500–600 °C under inert conditions (Figure 1). Each precursor yields distinct material properties: melamine polymerises into highly crystalline but low-surface-area C_3N_4 (<10 m^2 g^{-1}) [20], while urea gives rise to a porous network (up to 80 m^2 g^{-1}) with abundant defects that serve as active sites [21]. While melamine-derived C_3N_4 exhibits high thermal stability and corrosion resistance, its limited porosity restricts access to reactive sites [22]. In contrast, urea-based C_3N_4 features interlamellar channels and exposed edges that facilitate pollutant adsorption and electron transfer [23]. Dicyandiamide-derived C_3N_4, though less studied, offers intermediate conductivity and defect density, highlighting how precursor choice tailors functionality for specific applications [24]. These structural differences directly impact photocatalytic activity [6]. Additionally, mechanical and/or chemical exfoliation (e.g., ultrasound, microwave, hydrothermal or acid treatments) yields thin C_3N_4 nanosheets, increasing active surface area, maximising the exposure of new active sites [25–27].

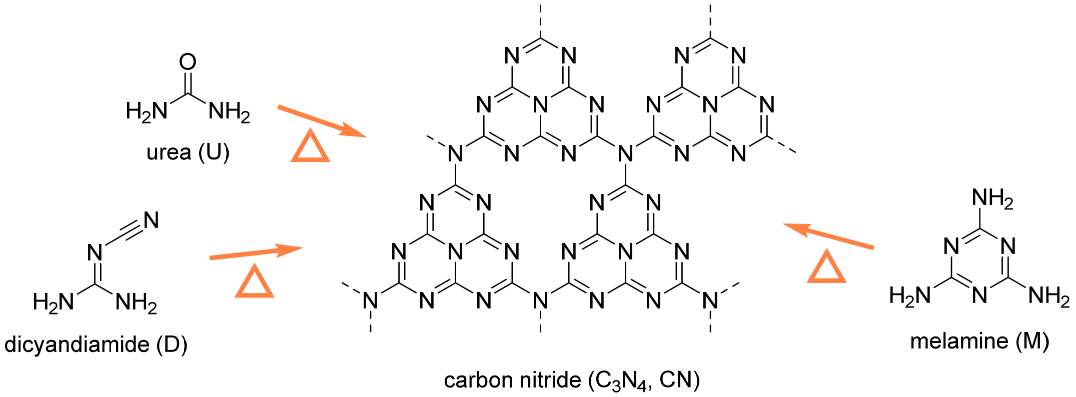

Figure 1. Structures of precursors used in this work (urea, dicyandiamide and melamine) for the synthesis of C_3N_4 by pyrolysis/polycondensation; codes employed in the text for each substance are indicated in brackets.

To enhance photocatalytic hydrogen evolution efficiency, a metallic co-catalyst is often deposited in the form of nanoparticles on the surface of C_3N_4 nanosheets [28–30]. One of the most successful modification strategies is platinum photodeposition, whereby Pt nanoparticles anchor in a highly dispersed fashion onto graphitic carbon nitride layer surfaces; such intimate contact reduces electron-hole recombination and catalyses proton reduction into H_2 [29–32].

This study offers a novel perspective on the development of photocatalysts based on graphitic carbon nitride by systematically analysing the influence of synthesis parameters including precursor type, exfoliation method, and platinum photodeposition conditions on both structural and photocatalytic performance. Unlike most previous works focused solely on dye degradation or model pollutants, this research directly links the physicochemical characteristics of C_3N_4-based materials to their activity in hydrogen production from oxygenated organic compounds that simulate wastewater components of increasing molecular complexity. By integrating synthesis optimization with application testing under solar-simulated conditions, the study bridges material development and real-world relevance, highlighting the dual role of these materials in clean energy generation and wastewater valorisation.

2. Experimental Section

2.1. Materials

Melamine (99%) and urea (98%) were acquired from Fisher Scientific (Madrid, Spain). Dicyandiamide (99%), hexachloroplatinic(IV) acid hydrate (w(Pt) ≥ 37.5%), poly(ethylene glycol) ($M_w = 400$ Da, PEG) and methanol (>99%) were acquired from Sigma-Aldrich (Madrid, Spain). D-(+)-Glucose (≥99.9%) was acquired from Labbox (Barcelona, Spain). Ethanol (96%) and glycerol (99.5%) were acquired from Scharlab (Barcelona, Spain). Nitrogen (≥99.9992%) was acquired from Carburos Metálicos (Barcelona, Spain). All chemicals were used as received without further purification.

2.2. Synthesis of C_3N_4 materials

2.2.1. Synthesis of bulk C_3N_4

Bulk carbon nitride (abbreviated as CN hereinafter) was synthesized via a modified thermal polymerization method in a semi-closed system by a procedure adapted from a report by Wang et al. [33]. In a typical procedure, the desired precursor (urea, melamine or dicyandiamide, 10 g) was placed in a 50 mL alumina crucible. The crucible was closed with a lid, tightly wrapped with two layers of aluminium foil and heated at a ramp rate of 5 °C min^{-1} up to 550 °C in a muffle furnace. The temperature was maintained for 3 h under static air conditions, followed by natural cooling to room temperature. The resulting bulk g-C_3N_4 was ground into fine powder using an agate mortar and designated as CN-U (urea-derived), CN-M (melamine-derived) or CN-D (dicyandiamide-derived).

2.2.2. Exfoliation of Bulk C_3N_4

Thermal exfoliation. Bulk CN-M (1 g) was placed in an uncovered ceramic crucible and heated at a ramp rate of 5 °C min^{-1} up to 500 °C, and then maintained at that temperature for 2 h, in static air. The resulting thermally exfoliated material was designated as CN-M^T. This annealing procedure led to a loss of ≈4% of the total initial mass.

Ultrasonic exfoliation. Bulk CN-M (1 g) was dispersed in 150 mL of ethanol/water mixture (25:75 *v*/*v*) and sonicated (35 kHz, Ultrasonic Bath, Sonorex Digitec DT 514 BH) for 10 h. The temperature was maintained at ≈30 °C in a water bath. The suspension was separated into precipitate and supernatant by centrifugation (4000 rpm, 5 min) and decantation. The supernatant fraction was dried by evaporating the solvent at 100 °C in an oven to yield a finer solid material (CN-M^{US}), whereas the precipitate was dried in an oven at 60 °C overnight, leaving a coarser solid fraction (CN-M^{UP}).

2.2.3. Co-Catalyst Photodeposition

Platinum was deposited on the CN samples using a modified photodeposition method adapted from Herrera et al. [31]. In a typical procedure, bulk CN-M (150 mg) was dispersed in an aqueous methanol or ethanol solution (30 mL, either 10% or 20% *v*/*v*) containing H_2PtCl_6 as the precursor, with platinum loadings calculated as 1 or 3% mass ratios relative to C_3N_4. The mixture was transferred to a quartz reactor and purged with nitrogen for 20 min to ensure an inert atmosphere. Photodeposition was achieved by exposing the mixture to UV lamp light (3UV Handheld series, 8 W) at 265 nm for 8 h. The resulting catalysts were collected by filtration and dried at 60 °C in an oven overnight. Samples were labelled as: $^{1\text{-}E20}$Pt-CN-X, $^{1\text{-}E10}$Pt-CN-X, $^{1\text{-}M20}$Pt-CN-X, $^{1\text{-}M10}$Pt-CN-X or $^{3\text{-}M10}$Pt-CN-X, where the prefix number indicates Pt loading (1 or 3%), 'E'/'M' denotes the alcohol used (ethanol or methanol, respectively), and the suffix number represents the alcohol concentration (10 or 20%). The final suffix (X) indicates the carbon nitride precursor and exfoliation method, where appropriate (see above).

2.2.4. Characterisation

The crystalline phases of the photocatalysts were identified by X-ray diffraction (XRD) performed on a Bruker D8-Discover diffractometer (Bruker, Karlsruhe, Germany) using Cu $K\alpha$ radiation (λ = 1.54 Å) at a 10 ° min^{-1} scanning rate over the 2θ diffraction angle range between 5 and 80 °. The morphology and the elemental composition of the photocatalysts were studied by scanning electron microscopy (SEM) using a Quanta 600-FEI microscope (FEI, Hillsboro, OR, USA). The size and distribution of platinum co-catalyst particles were examined by means of transmission electron microscopy (TEM) using a JEOL-1011 microscope (JEOL, Tokyo, Japan), operating at 100 kV. Platinum co-catalyst nanoparticle sizes were measured as projected diameters from TEM images using the Image J software (National Institutes of Health, Bethesda, MD, USA). Optical characterization of the materials was conducted by diffuse reflectance spectroscopy (DRS) using Cary 5000 UV-Vis-NIR spectrophotometer (Agilent Technologies, Santa Clara, CA, USA) equipped with a praying mantis sample accessory, using $BaSO_4$ as the reference material. The structural features of the photocatalysts were examined by means of attenuated total reflectance Fourier transform infrared spectroscopy (ATR-FTIR), recorded on a Jasco FT/IR instrument (JASCO, Tokyo, Japan).

2.2.5. Photocatalytic Hydrogen Production Experiments

Hydrogen production experiments via photoreforming were conducted in batch mode using suspensions of a photocatalyst (20 mg) in aqueous solutions (25 mL) of methanol, glucose, glycerol or poly(ethylene glycol) (PEG) (10, 5, 2 or 1% *w*/*v*) inside a gas-tight quartz reactor. In some cases, pH was adjusted using aqueous NaOH or HCl solutions. Otherwise, irradiations were performed under unaltered pH (ca. 6.5 for methanol). The photoreaction occurs under a nitrogen atmosphere and simulated solar light (Xe lamp, AM1.5G, 100 mW cm^{-2}, Oriel Instruments, Stratford, CT, USA). Gas samples (2 mL) were analysed on a two-channel chromatograph (Agilent 990 Micro GC Systems, Agilent Technologies, Santa Clara, CA, USA): one channel was equipped with a thermal conductivity detector (TCD), a MS 5 Å column, using argon as the carrier gas, for the quantification of H_2, O_2 and N_2; the second channel was equipped with PoraPLOT Q column for the quantification of CO_2 and hydrocarbons using helium as the carrier gas. Error bars in gas productions were determined (ca. ± 5%) as the standard deviation from triplicate experiments in selected cases.

3. Results and Discussion

3.1. Effects of Precursor on C_3N_4 Structure and Morphology

The influence of the nitrogen precursor on the morphology of the resulting C_3N_4 materials was investigated using three distinct precursors: urea, dicyandiamide and melamine (Figure 1). All materials were synthesised via thermal polymerisation (polycondensation) of the precursors. Their crystallinity was analysed by X-ray diffraction (Figure 2). The diffractograms confirm the expected carbon nitride structure. A weak diffraction peak observed at $2\theta = 13.1$ ° is associated with the diffraction along the (100) direction, corresponding to the in-plane periodicity of the tri-s-triazine units in the graphite-like layered structure [2,34,35]. Conversely, the intense diffraction peak at approximately 27.3 ° corresponds to the diffraction caused by the (002) planes related to interlayer stacking of the conjugated aromatic system [2,34,35].

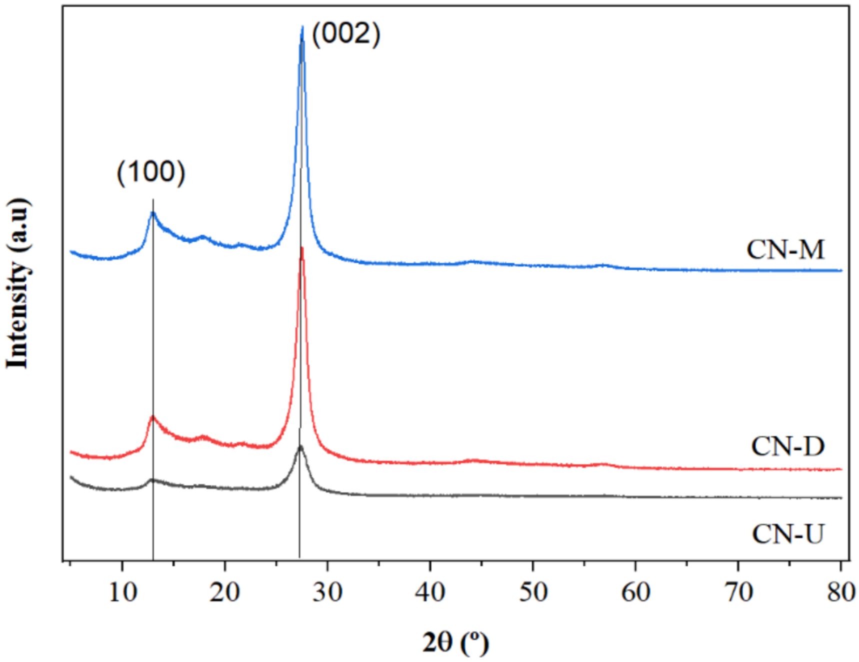

Figure 2. XRD patterns of C_3N_4 prepared from different precursors. Main diffraction signals are labelled as the corresponding Miller indices.

The comparison of the peak intensities corresponding to the (100) plane provides insight into the degree of nanosheet growth and crystallinity of the carbon nitride sheets within the material. It can be inferred that CN-U exhibits a more amorphous nature or smaller particle size, evidenced by the low intensity and broadness of its diffraction peaks. In contrast, the CN-M and CN-D materials display a higher crystallinity, indicative of more extensive and effective polymerisation, as their (100) plane peaks are well-defined and more intense than those of CN-U.

The higher crystallinity of C_3N_4 synthesized from precursors such as melamine or dicyandiamide (compared to urea) is attributed to structural and kinetic differences during thermal polymerization. The triazine rings (C_3N_3) and their pendant amino groups (–NH_2) in melamine, or the cyanamide groups (=N–C≡N) in dicyandiamide are more structurally similar to the heptazine units (C_6N_7) of the final product backbone. This facilitates direct and ordered condensation via C–N bond formation, minimizing molecular rearrangements and promoting layer growth. In contrast, urea has a simpler structure that undergoes multistep thermal decomposition (forming intermediates, including melamine) before polymerization. This process introduces structural defects and releases volatile by-products (e.g., NH_3, CO_2, H_2O), creating porosity. Furthermore, rapid decomposition of urea at relatively low temperatures leads to chaotic polymerization kinetics, whereas the thermal stability of melamine and dicyandiamide enables gradual, controlled condensation, reducing void formation [34,36].

Nanosheet morphology of the C_3N_4 materials prepared from different precursors was studied by TEM (Figure 3, top). Micrographs corresponding to CN-U reveal a two-dimensional structure consisting of flat sheets with wrinkles and irregular shapes, along with visible discontinuity within the layers, demonstrating its lighter and more porous nature. In contrast, both CN-M and CN-D materials show non-porous layered structures. Specifically, CN-M exhibits smooth, well-stacked sheets, while CN-D displays irregularly shaped and wrinkled layers. Moreover, SEM micrographs of CN-M, CN-D and CN-U materials revealed distinct morphological differences attributable to their respective polymerization mechanisms (Figure 3, bottom). The CN-M material displays a compact structure with well-defined, densely stacked layers, consistent with the aforementioned ordered polycondensation mechanism of melamine as its precursor. In contrast, CN-D exhibits irregular dense surfaces with increased roughness and particle size heterogeneity compared to CN-M. This morphological behaviour stems from the presence of cyanamide groups in dicyandiamide, which, while enabling direct condensation, results in less structural uniformity due to slightly less controlled polymerisation mechanisms. The CN-U material exhibits markedly different characteristics, featuring a highly porous morphology with small, irregularly distributed particles. This observation aligns consistently with both XRD and TEM results, confirming the disordered structural nature of the urea-derived material.

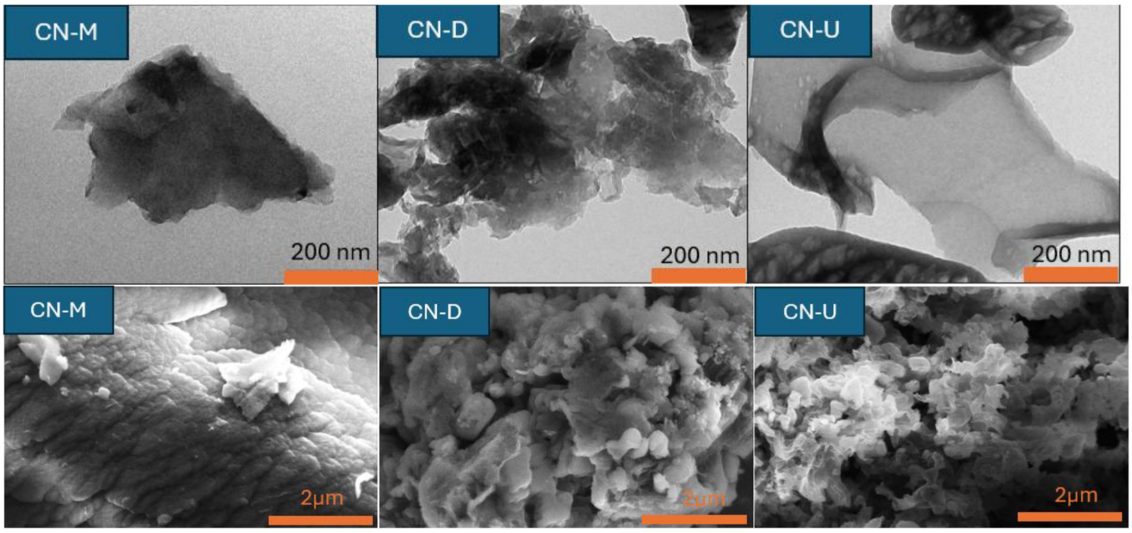

Figure 3. TEM (**top**) and SEM (**bottom**) micrographs of C_3N_4 prepared from different precursors.

The chemical structure of the synthesized carbon nitride materials was studied by ATR-FTIR spectroscopy (Figure S1). The spectra showed characteristic absorption bands between 1200–1650 cm^{-1}, consistent with reported literature values for similar materials [26,35]. Distinct peaks observed at 1640, 1569, 1412, 1326, and 1240 cm^{-1} were assigned to vibrational stretching modes of C=N and C-N bonds [35,37]. A broad absorption band in the 3000–3400 cm^{-1} region was attributed to N-H stretching vibrations due to terminal NH or NH_2 groups, and trace amounts of adsorbed water molecules. Notably, CN-U exhibited high intensity in this region (Figure S1) suggesting more -NH or -NH_2 terminal groups [26,35,37]. All samples displayed a strong peak at 815 cm^{-1}, representing the out-of-plane bending vibration characteristic of heptazine rings [37], which confirms the successful formation of the C_3N_4 structure. These spectroscopic results provide complementary evidence to support the structural differences observed in XRD and TEM analyses.

The UV-Vis diffuse reflectance spectra of the synthesized materials are presented in Figure S2. The band gaps were determined using the Tauc plot method with the Kubelka-Munk function. All materials exhibited semiconductor behaviour with band gaps ranging between 2.6 and 2.8 eV [4,5]. While CN-D and CN-M showed similar band gap values (≈2.7 eV), a significant wider band gap was observed for CN-U (≈2.8 eV). This variation can be attributed to structural differences between the samples. The more complete polymerization and ordered structure in CN-D and CN-M facilitate delocalized electron mobility, resulting in narrower band gaps. In contrast, the increase in the band gap of CN-U is attributed to the degree of polymerization, which governs the crystallinity and size of C_3N_4 sheets. Smaller sheets lead to reduced orbital delocalization, resulting in a larger band gap due to quantum confinement effects [9,34]. Moreover, CN-M exhibited stronger light absorption, most notably in the entire visible range, as compared to CN-U and CN-D.

3.2. Effects of Exfoliation Method on C_3N_4 Structure and Morphology

The X-ray diffraction (XRD) patterns in Figure S3 reveal the crystalline structure of C_3N_4 nanosheets prepared through different exfoliation methods. All samples maintain the two characteristic peaks of the bulk CN-M material, confirming their structural integrity as graphitic carbon nitride. However, detailed analysis shows some modifications: the (100) peak intensity is reduced in all exfoliated samples, reflecting decreased in-plane layer dimensions due to fragmentation during processing. Conversely, the (002) diffraction peak shows a systematic shift toward slightly higher angles for the CN-M^T, CN-M^{UP}, and CN-M^{US} samples (Figure S3), indicating a contraction in interlayer spacing (d-spacing) that suggests enhanced interlayer interactions [26,38]. This structural compression likely results from a combination of factors including partial nanosheet restacking, induced defects, and surface functionalization during the exfoliation process.

Figure 4 displays SEM micrographs of exfoliated C_3N_4 materials. As discussed earlier, bulk C_3N_4 synthesized from melamine typically exhibits a dense and uniform structure. In contrast, the exfoliated samples show distinct morphological changes:

- CN-M^T: Displays smaller particle sizes than CN-M, with wrinkled and curled edges due to surface energy minimization [39].
- Ultrasonically exfoliated samples (CN-M^{UP} and CN-M^{US}) exhibit lamellar morphologies with slightly reduced particle dimensions. Specifically, CN-M^{US} reveals loosely packed, crumpled nanosheets, attributed to the disruption of van der Waals forces between C_3N_4 layers under intense ultrasonic waves [26].

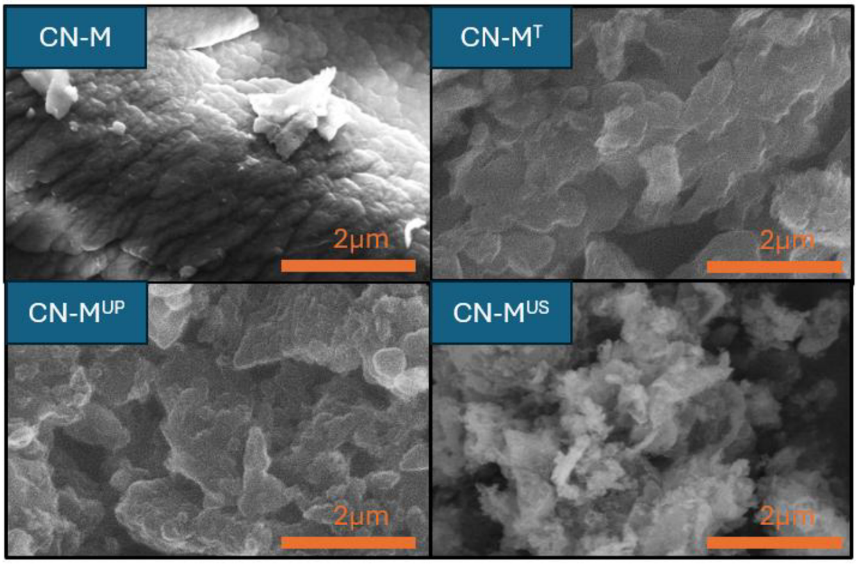

Figure 4. SEM micrographs of exfoliated C_3N_4 materials.

All exfoliated materials exhibit thinner layers compared to the pristine CN-M material (see Section 3.3 below). In the case of CN-M^T, thin sheets of similar size to those observed in CN-M can be seen. On the other hand, CN-M^{UP} and CN-M^{US} materials show smaller sheets. For CN-M^{UP}, these nanosheets appear stacked, while CN-M^{US} displays more separated and fragmented layers.

The light absorption properties of C_3N_4 materials prepared using different exfoliation methods were studied by UV-Vis diffuse reflectance spectroscopy. As shown in Figure S4, CN-M^T and CN-M^{UP} materials exhibit a blue shift in their absorption edges compared to the CN-M sample. This shift can be attributed partly to quantum confinement effects arising from the nanosheet structure and partly to changes in band edge positions due to reduced conjugation [26]. The band gap energies of the exfoliated C_3N_4 materials were estimated as discussed in the previous section. The band gaps marginally increased from 2.70 eV for CN-M to 2.71 eV and 2.73 eV for CN-M^T and CN-M^{UP}, respectively. However, CN-M^{US} showed significantly more intense absorption across both the UV and visible ranges, and a reduced band gap of 2.62 eV, which indicates enhanced visible light absorption capacity.

3.3. Disperisty of Photodeposited Pt Co-Catalyst Nanoparticles

The effect of photodeposition conditions on platinum nanoparticle formation was evaluated using 1% and 3% Pt loadings while varying both the sacrificial agent (methanol or ethanol) and its concentration (10% or 20% *v*/*v*). Although lower platinum ratios might prove beneficial in both performance and economic terms, and will be investigated in further optimisations, the studied range was considered to have a first insight into loading effects. The XRD patterns of the platinum-modified materials (Figure S5) confirm that the photodeposition process preserves the crystalline structure of the C_3N_4 supports. For materials loaded with 3% Pt, a distinct peak at 39.9 ° corresponding to the (111) plane of metallic platinum was observed, while this peak was absent in the 1% Pt samples due to the lower concentration and higher dispersion of nanoparticles below the XRD detection limit.

The photodeposited Pt nanoparticles showed relatively fine dispersion and little or no significant aggregate formation on the surface in Pt-CN-M materials with a 1% Pt/C_3N_4 mass ratio, as observed by TEM (sizes around or slightly below 2 nm, Figure 5). Nevertheless, some Pt nanoparticle clustering can be observed for $^{1\text{-}M10}$Pt-CN-M and related materials on exfoliated C_3N_4. By increasing the content of platinum, differences become clear. Higher Pt loading resulted in a multimodal size distribution (e.g., $^{3\text{-}M10}$Pt-CN-M, Pt nanoparticle sizes distributed into two main groups of 1.8 ± 0.5 and 16 ± 4 nm, Figure 5) and an obvious, massive, nanoparticle aggregation, whereas the counterpart with 1% Pt by mass exhibited well-dispersed Pt nanoparticles on the surface of C_3N_4 nanosheets ($^{1\text{-}M10}$Pt-CN-M, 2.0 ± 0.6 nm). Thus, lower Pt loading resulted in higher dispersity, and hence, more accessible Pt/C_3N_4 interfaces. This uniform distribution is expected to enhance charge separation and provide abundant active sites for hydrogen evolution. Moreover, using ethanol as the sacrificial agent led to a higher number nanoparticles into a remarkably uniform size distribution (1.4 ± 0.5 nm, see $^{1\text{-}E10}$Pt-CN-M micrograph in Figure 5), presumably generating more active sites compared to methanol-based deposition. However, increasing the ethanol concentration to 20% results in a broader nanoparticle dispersity (1.7 ± 0.6 nm, $^{1\text{-}E20}$Pt-CN-M), likely due to competitive adsorption effects at higher molar concentrations of alcohol, resulting in similar co-catalyst distribution to that in materials prepared in 10% aqueous methanol (e.g., $^{1\text{-}M10}$Pt-CN-M, see Figure 5).

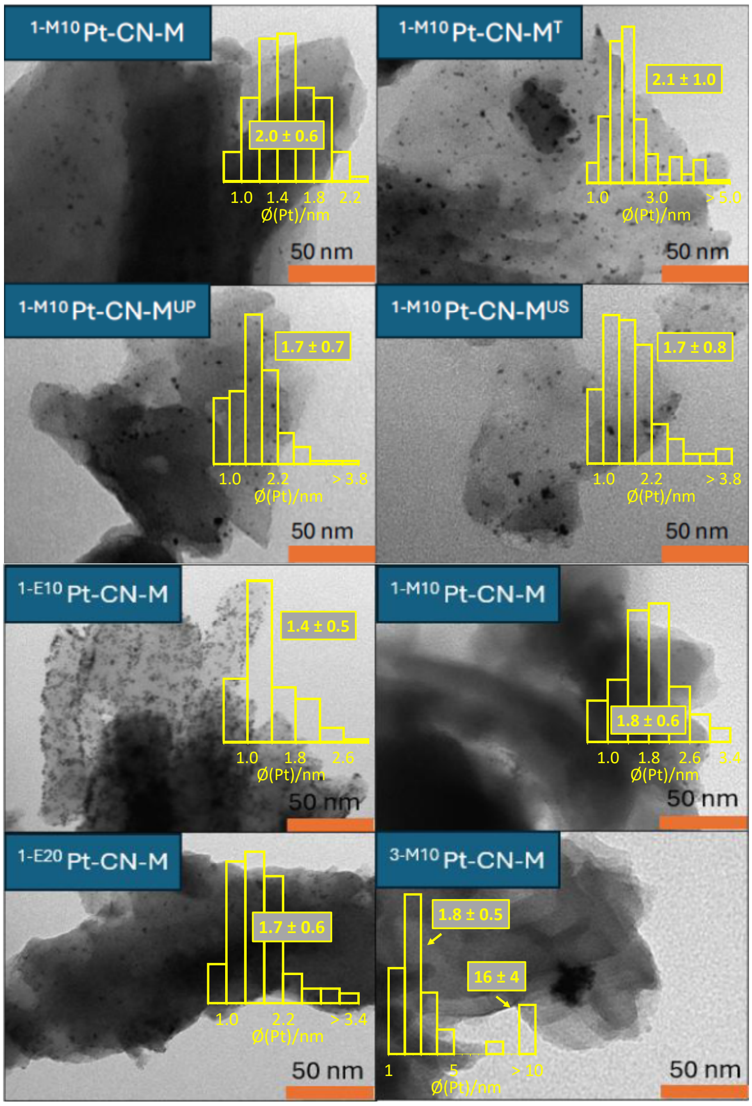

Figure 5. TEM micrographs of Pt-CN-M materials after platinum photodeposition performed by a variation of the general procedure. Insets: Pt nanoparticle size distribution histograms; data in boxes indicate average and standard deviation values.

The UV-Vis diffuse reflectance spectra of the materials revealed that the Pt-containing samples exhibited slightly enhanced light absorption across the UV range, and extending as tails into the visible, as compared to the Pt-free counterparts (Figure S6). These results suggest that platinum nanoparticles may facilitate and enhance light absorption efficiency, either by plasmon resonance, dielectric scattering [40], or via d-d transitions [32,41].

3.4. Photocatalytic Hydrogen Production

3.4.1. Effect of C_3N_4 Morphology and Reaction Conditions (pH)

The photocatalytic hydrogen production performance of non-exfoliated carbon nitride materials synthesized from different precursors (melamine, dicyandiamide or urea) containing photodeposited platinum nanoparticles was systematically evaluated using methanol as the substrate. As shown in Figure 6, after four hours of irradiation, the melamine-derived material ($^{1\text{-M}10}$Pt-CN-M) exhibited significantly higher hydrogen evolution efficiency compared to both $^{1\text{-M}10}$Pt-CN-D and $^{1\text{-M}10}$Pt-CN-U samples. An initial induction time was obvious in all cases, probably due to substrate binding and/or activation steps at the beginning of the process. This enhanced activity can be attributed to the combined effect of its superior crystallinity, which promotes efficient electron mobility through delocalized π-conjugated systems (as discussed in Section 3.1), and its optimal band gap (2.65 eV) that facilitates visible light absorption. In contrast, despite its higher porosity and theoretically larger surface area, the urea-derived $^{1\text{-M}10}$Pt-CN-U material showed the lowest photocatalytic activity. This reduced performance likely stems from its structural defects acting as charge recombination centres, lower crystallinity impairing electron transport and wider band gap (2.78 eV) limiting light absorption. The activity of dicyandiamide-derived $^{1\text{-M}10}$Pt-CN-D was similar to that of the urea-derived counterpart despite showing similar structural features to the best-performing melamine-derived material (see XRD and ATR-FTIR in Figures 2 and S1, respectively). This indicates that the irregular and wrinkled surfaces of CN-D and CN-U, as opposed to the smoother and more effectively layered morphology of CN-M (Figure 3), could be detrimental to photocatalytic activity. Another possible reason for the higher performance of $^{1\text{-M}10}$Pt-CN-M could be its extended visible light absorption (Figure S2).

These results clearly demonstrate how the choice of nitrogen/carbon precursor critically determines the structural and electronic properties of the resulting carbon nitride, which in turn governs its photocatalytic efficiency for hydrogen production. Based on these findings, melamine was selected as the optimal precursor for subsequent studies investigating exfoliation processes, as it provides the best combination of crystallinity, appropriate nanosheet morphology, band structure, and visible light response among the tested materials.

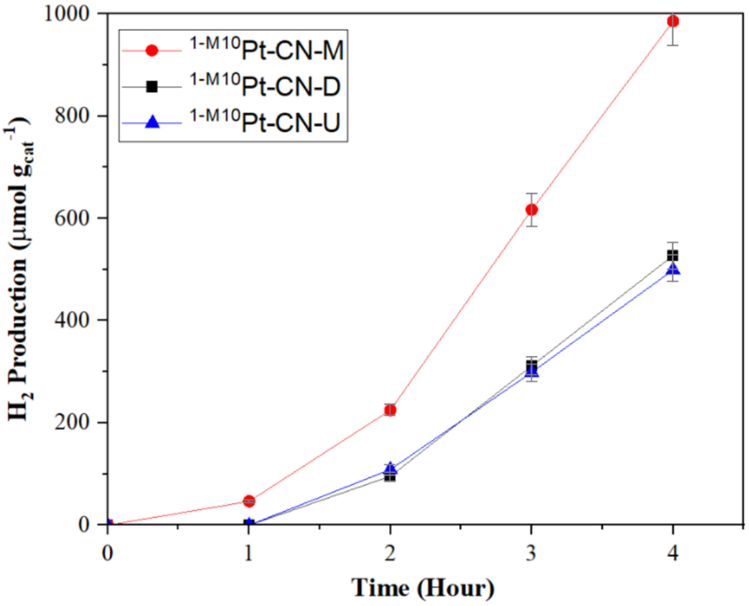

Figure 6. Effect of catalyst precursor on the photocatalytic production of hydrogen using Pt-CN-*X* (20 mg; *X* = M, D, U) dispersed in aqueous methanol (10% *v*/*v*), under simulated sunlight (Xe lamp, AM1.5G, 1000 W m^{-2}) and nitrogen atmosphere.

The pH of the reaction medium represents a critical operational parameter that significantly influences hydrogen production by photoreforming. A systematic evaluation of the efficiency of $^{1\text{-M}10}$Pt-CN-M as a photocatalyst under controlled conditions revealed a complex pH-dependence that directly correlates with both the material surface chemistry and the reaction thermodynamics (Figure 7). Photocatalytic activity can be influenced by multiple factors depending on pH, such as (*i*) H^+ concentration; (*ii*) maintenance of the -NH-/=N- groups in their unprotonated, catalytically active state; (*iii*) electrostatic agglomeration of particles if the pH approaches the point of zero charge (pH = 4–5, [42,43]); and (*iv*) oxidation potentials of the substrates, which tend to be more negative at increasing pH. Under neutral conditions (pH range: 6–8), $^{1\text{-M}10}$Pt-CN-M achieves optimal hydrogen evolution due to sufficient proton availability, preserved catalyst integrity and dispersion, and favourable oxidation thermodynamics. In acidic media, hydrogen production was up to 40% lower than under neutral conditions, probably due to agglomeration and/or protonation of nitrogen atoms.

Operation in the alkaline regime resulted in greatly variable behaviour. An activity decline was observed at pH = 9, whilst hydrogen evolution was noticeably higher (although lower than under neutral conditions) at pH = 12. While increasing alkalinity represents a decrease in the concentration of H^+, strongly basic conditions activate alternative advantageous pathways due to enhanced oxidative activity. Most notably, the methanol oxidation process, which plays a critical role in hole reduction, exhibits pH-dependent oxidation potential. Under alkaline conditions (high pH), the reaction occurs at a lower oxidation potential (−0.82 and +0.02 V vs. the standard hydrogen electrode, at pH = 0 or 14, respectively), thereby facilitating oxidative degradation by photoreforming [44]. Ultimately, faster oxidation half-reaction would prompt a more efficient H_2 evolution. These results demonstrate that CN-M materials can be effectively utilized for treating neutral or strongly alkaline wastewater streams without requiring pH adjustment.

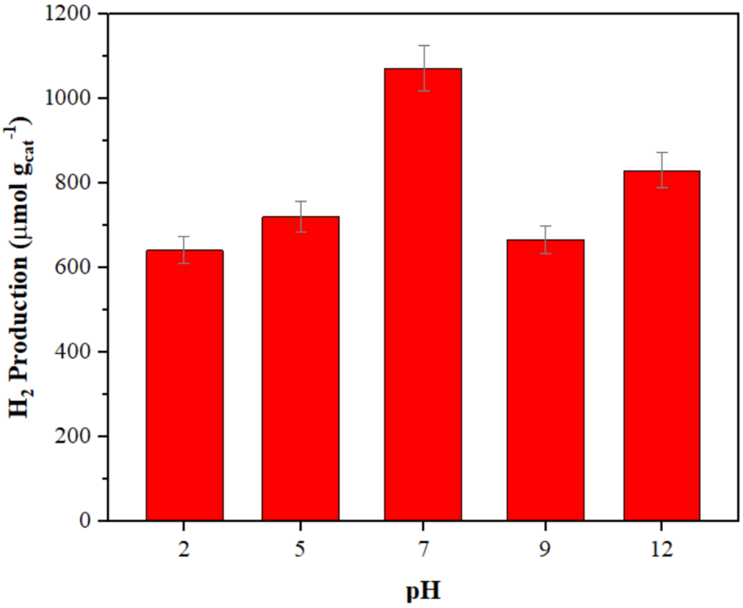

Figure 7. Effect of pH on hydrogen production using $^{1\text{-M}10}$Pt-CN-M photocatalyst dispersed in aqueous methanol (10% *w*/*v*), under simulated sunlight (Xe lamp, AM1.5G, 1000 W m^{-2}) and nitrogen atmosphere after 4 h.

The hydrogen production performance of exfoliated carbon nitride materials was compared to that of the pristine $^{1\text{-M}10}$Pt-CN-M (Figure 8). All exfoliated C_3N_4 photocatalysts showed increased photocatalytic activity. The ultrasonically treated $^{1\text{-M}10}$Pt-CN-M^{UP} and $^{1\text{-M}10}$Pt-CN-M^{US} materials exhibited the most remarkable enhancement (ca. 40%). The CN-M^{US} sample was particularly outstanding, demonstrating detectable hydrogen evolution within the first hour of irradiation—a clear indicator of its rapid photocatalytic activation. This exceptional performance stems from the unique structural and morphological modifications induced by ultrasonic exfoliation. The intense cavitation effects generated ultra-thin nanosheets with substantially increased surface area and active sites (Figure 4). Importantly, $^{1\text{-M}10}$Pt-CN-M^{US} showed reduced layer stacking compared to $^{1\text{-M}10}$Pt-CN-M^{UP} (as evidenced by TEM, see Figure 5), which significantly improved reactant accessibility to catalytic sites. Furthermore, the parent CN-M^{US} exhibited the most beneficial band gap reduction pristine CN-M (2.62 vs. 2.70 eV, Figure S4), enabling extended visible light harvesting.

Albeit the thermally exfoliated $^{1\text{-M}10}$Pt-CN-M^{T} showed measurable structural changes (Section 3.2), its photocatalytic performance remained similar to that of the non-exfoliated counterpart, $^{1\text{-M}10}$Pt-CN-M, likely due to insufficient modification of both surface area and electronic properties. These results highlight ultrasonic exfoliation as a particularly effective approach for enhancing the hydrogen production capabilities of carbon nitride, with $^{1\text{-M}10}$Pt-CN-M^{US} emerging as the optimal photocatalyst due to its synergistic combination of improved nanosheet morphology, enhanced surface area, and favourable electronic structure modifications that collectively boost photocatalytic efficiency.

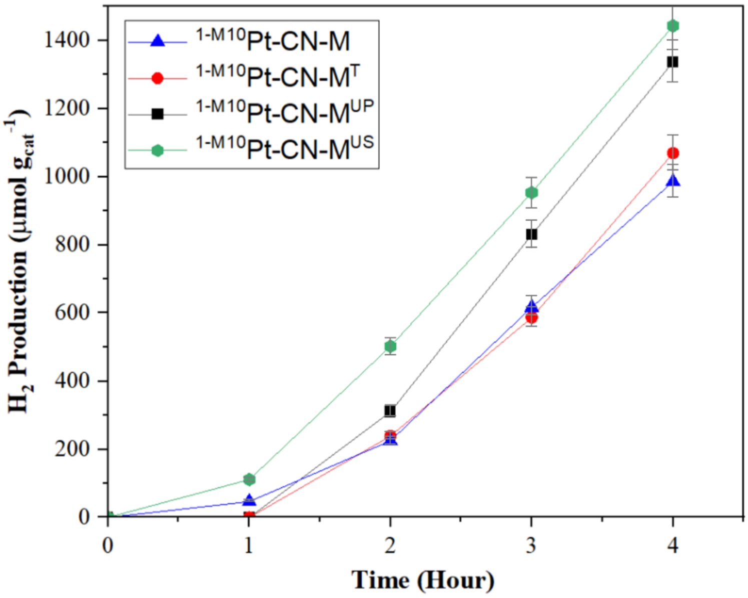

Figure 8. Effect of exfoliation method on hydrogen production using $^{1\text{-}M10}$Pt-CN-M photocatalysts from aqueous methanol (10% *w*/*v*) under simulated sunlight (Xe lamp, AM1.5G, 1000 W m^{-2}) and nitrogen atmosphere.

3.4.2. Effect of Pt Dispersity

Systematic study of parameters influencing platinum nanoparticle photodeposition on carbon nitride revealed dramatic effects of conditions on photocatalytic activity (Figure 9). The results showed that the material with the highest metal loading (3% by weight, $^{3\text{-}M10}$Pt-CN-M) did not result in increased hydrogen production yield as compared to $^{1\text{-}M10}$Pt-CN-M, an effect attributable to metal agglomeration, as observed by TEM (Figure 5). This reduces the number of accessible active sites due to decreased surface-to-volume ratios and offsets the higher amount of bulk platinum, compared to much more favourable distribution of well-dispersed nanoparticles for materials with 1% metal content.

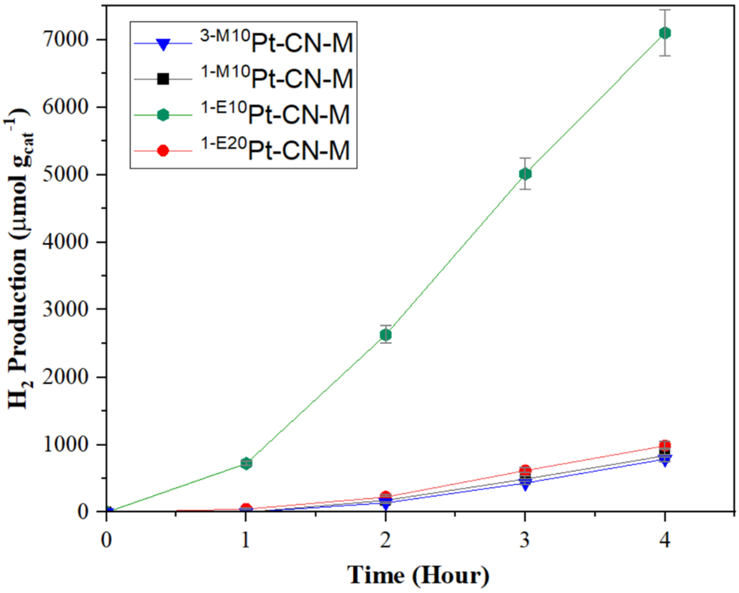

Figure 9. Effect of platinum nanoparticle photodeposition parameters on hydrogen production from aqueous methanol (10% *w*/*v*) under simulated sunlight (Xe lamp, AM1.5G, 1000 W m^{-2}) and nitrogen atmosphere.

Additionally, the effect of the reducing agent used during Pt photodeposition shows that using 10% ethanol ($^{1\text{-}E10}$Pt-CN-M) greatly increased hydrogen production (by a seven-fold factor up to ca. 7.0 mmol g^{-1}, see Figure 9) as compared to analogous materials prepared with methanol ($^{1\text{-M}10}$Pt-CN-M). One possible reason for this enhancement is the higher reducing potential of ethanol (−0.33 V vs. the standard hydrogen electrode) that favours faster and more uniform nucleation of Pt nanoparticles, as well as its preferential adsorption at specific sites on C_3N_4 that promotes homogeneous distribution. In fact, the major morphological improvement in terms of Pt dispersity was observed for $^{1\text{-E}10}$Pt-CN-M (see Figure 5). However, when increasing ethanol concentration to 20% ($^{1\text{-E}20}$Pt-CN-M), hydrogen production decreased significantly. These findings directly correlate with microscopy analyses reported in Section 3.3, which confirmed that $^{1\text{-E}10}$Pt-CN-M had the highest nanoparticle density and dispersity with uniform distribution, whereas platinum nanoparticles tended to grow larger and cluster to some extent in $^{1\text{-E}20}$Pt-CN-M, in turn leading to drastically lower hydrogen evolution. These results establish that the optimal metal loading is 1% by weight using 10% *v*/*v* ethanol as a reducing agent, thus providing clear guidelines for designing highly efficient metal-based photocatalysts.

3.4.3. Effect of Type of Oxygenated Substrate

The photocatalytic performance of $^{1\text{-M}10}$Pt-CN-M$^{\text{US}}$ carbon nitride was systematically evaluated for hydrogen production using three model oxygenated substrates, namely glucose, glycerol and polyethylene glycol (PEG) under simulated solar irradiation (Figure 10). After one day of continuous operation, all systems demonstrated measurable hydrogen evolution, though with significant variations in production rates that reflect fundamental differences in substrate degradability and reaction pathways. It should be noted that mass transfer limitations are expected to be minimal at the studied concentrations, since viscosities are similar or, at most, marginally higher than that of pure water [45]. For example, the viscosity of a 2% *w*/*v* aqueous PEG solution is ca. 0.97 mPa s, as compared to 0.89 for water [46]. Glycerol emerged as the most effective sacrificial agent, achieving the highest hydrogen production yield of (>1.8 mmol g^{-1}). This superior performance directly correlates with its simple triol structure and low oxidation potential, which facilitate rapid dehydrogenation kinetics through direct hole-mediated oxidation [47]. The added difficulty in cleaving C-C or C-O bonds in the more complex glucose and PEG structures may also be a critical factor, partly hindering performance. The process readily liberates protons for subsequent reduction to H_2.

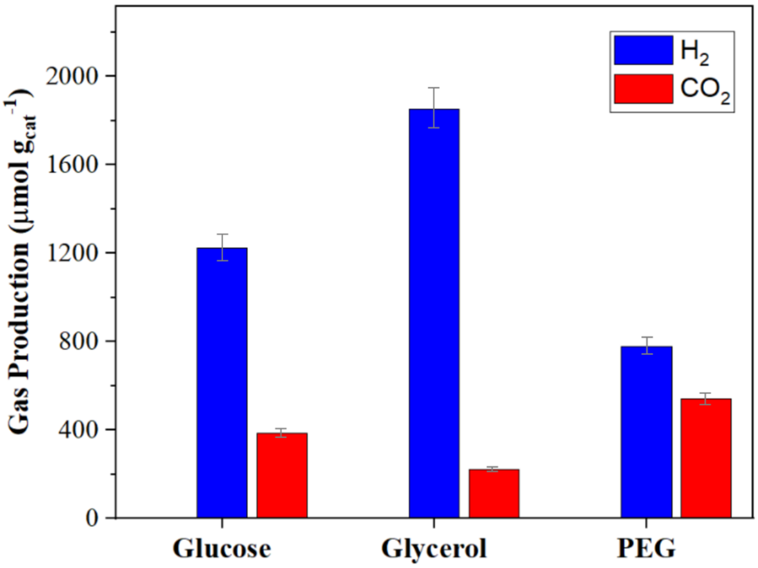

Figure 10. Hydrogen production with three different substrates using $^{1\text{-M}10}$Pt-CN-M$^{\text{US}}$ photocatalyst (concentrations of glucose, glycerol and PEG were 5, 2 and 2% *w*/*v*, respectively) under simulated sunlight (Xe lamp, AM1.5G, 1000 W m^{-2}) and nitrogen atmosphere for 24 h.

In contrast, glucose showed approximately 34% lower hydrogen production, a consequence of its more complex cyclic saccharide structure that requires ring-opening steps before complete oxidation can occur [48,49]. Interestingly, while PEG exhibited the lowest hydrogen evolution (778 μmol g^{-1}), it led to the highest CO_2 production (541 μmol g^{-1}), indicating the mineralisation of this polymeric substrate. This apparent contradiction reveals important mechanistic insights: the degradation of PEG follows a distinct two-stage process where initial random chain scission generates intermediate fragments that subsequently undergo deep oxidation, with most carbon ultimately evolving as CO_2 in parallel to hydrogen production [50,51]. In fact, molar H_2/CO_2 ratios are lower to that defined by the theoretical reaction stoichiometry (5:2). By contrast, the simpler monomeric alcohol, polyol and saccharide substrates result in H_2/CO_2 ratios noticeably higher than stoichiometric, indicating a step-wise mechanism initiated by dehydrogenation and formation of oxidation intermediates [28].

These results reported herein represent a development over previous reports, given the variability of oxygenated organic substrates tested, and the H_2 production rates obtained. Our results imply a one-order-of-magnitude optimisation from ca. 200 μmol g^{-1} h^{-1} to nearly 2 mmol g^{-1} h^{-1} for the specific case of methanol as substrate (see Table 1). As compared to literature results, this is close to the highest efficiency under standard simulated sunlight (AM1.5G, 2.81 mmol g^{-1} h^{-1}, reference [52]). Similar or higher production rates have been reported, but employing high-power concentrated irradiation, for photocatalytic hydrogen production using methanol, glycerol or glucose as substrates (see Table 1). Therefore, our investigations carry significant implications for wastewater valorisation strategies. The $^{1\text{-}M10}$Pt-CN-M^{US} photocatalyst demonstrates versatility to handle diverse organic contaminants, from simple polyols to complex polymers, though with clearly differentiated reaction rates and product distributions.

Table 1. Summary of relevant literature results on photocatalytic hydrogen production using Pt/C_3N_4 materials as compared to those reported herein.

Photocatalyst	Substrate	Concentration	Light Source	H_2 Production Rate (μmol g^{-1} h^{-1})	Ref.
$^{0.5}$Pt/CN	MeOH	10% *v*/*v*	Xe lamp, 300 W, >420 nm [a]	30	[2]
^{1}Pt/CN	MeOH	20% *v*/*v*	Xe lamp, 350 W, >400 nm, 380 mW cm^{-2}	762	[53]
^{1}Pt/CN	MeOH, KOH	20% *v*/*v*, pH = 13	Xe lamp, 350 W, >400 nm, 380 mW cm^{-2}	2210	[53]
^{2}Pt/CN [b]	MeOH	10% *v*/*v*	Xe lamp, AM1.5G	2810	[52]
^{3}Pt/CN	MeOH	20% *v*/*v*	Xe lamp, >420 nm [a]	420	[54]
^{3}Pt/CN	MeOH	50% *v*/*v*	Xe lamp, 300 W [a,c]	$17.1\ 10^3$	[55]
$^{1\text{-}M10}$Pt-CN-M	MeOH	10% *w*/*v*	Xe lamp, AM1.5G, 100 mW cm^{-2}	245	this work
$^{1\text{-}M10}$Pt-CN-M^{US}	MeOH	10% *w*/*v*	Xe lamp, AM1.5G, 100 mW cm^{-2}	358	this work
$^{1\text{-}E10}$Pt-CN-M	MeOH	10% w/v	Xe lamp, AM1.5G, 100 mW cm^{-2}	1775	this work
$^{0.5}$Pt/CN	glycerol	10% *v*/*v*	LED, 450 nm, 325 mW cm^{-2}	540	[56]
$^{1\text{-}M10}$Pt-CN-M^{US}	glycerol	2% *w*/*v*	Xe lamp, AM1.5G, 100 mW cm^{-2}	77	this work
^{1}Pt-CN	glucose	5% *w*/*v*	LED, 440 nm, 580 mW cm^{-2}	50	[57]
$^{1\text{-}M10}$Pt-CN-M^{US}	glucose	5% *w*/*v*	Xe lamp, AM1.5G, 100 mW cm^{-2}	51	this work
$^{1\text{-}M10}$Pt-CN-M^{US}	PEG	2% *w*/*v*	Xe lamp, AM1.5G, 100 mW cm^{-2}	33	this work

[a] No irradiance reported. [b] Carbon nitride modified with pendant urea groups. [c] Irradiation system (Ceaulight Co., Ltd. (Beijing, China), CEL-HXF300-T3) provides concentrated light energy, according to the manufacturer, irradiances up to 2000 mW cm^{-2}.

4. Conclusions

The choice of precursor, exfoliation method and platinum deposition conditions significantly influence the structural, electronic and photocatalytic properties of C_3N_4. Melamine-derived photocatalysts (e.g., $^{1\text{-}M10}$Pt-CN-M) exhibited higher crystallinity and hydrogen production efficiency by methanol photoreforming under simulated sunlight irradiation, attributed to their ordered structure and optimal bandgap (2.65 eV), while the urea-derived material ($^{1\text{-}M10}$Pt-CN-U) showed lower activity due to its high porosity and structural defects. Ultrasonic exfoliation ($^{1\text{-}M10}$Pt-CN-M^{US}) emerged as the most effective method to enhance H_2 production, producing thin nanosheets with increased surface area and a reduced bandgap (2.62 eV), enhancing visible light absorption and charge separation. The effect of Pt co-catalyst dispersity was significantly more decisive. Photodeposition using 10% ethanol ($^{1\text{-}E10}$Pt-CN-M) resulted in smaller nanoparticle sizes (1.4 ± 0.5 nm) and finer dispersion than using 10% methanol (2.0 ± 0.6 nm), maximizing active sites and boosting H_2 production (7-fold increase up to ca. 7 mmol g^{-1} after 4 h), whereas higher Pt loading (3%) led to agglomeration and reduced performance.

In practical applications, $^{1\text{-}M10}$Pt-Pt-CN-M^{US} proved versatile for hydrogen production from model wastewaters containing structurally diverse oxygenated substrates. Increasing structural complexity and molecular mass, from a simple alcohol (methanol), through a polyol (glycerol), a monomeric saccharide (glucose) and an oligomeric polyglycol (PEG), hinders hydrogen evolution. Furthermore, the pH of the medium significantly affected photocatalytic activity, peaking under neutral conditions and showing notable performance in strongly alkaline environments (pH = 12) due to changes in oxidation reaction thermodynamics. These findings highlight the potential of modified C_3N_4 as a sustainable material for integrating wastewater treatment with clean energy generation, addressing both environmental and energy challenges simultaneously.

Supplementary Materials

The additional data and information can be downloaded at: https://media.sciltp.com/articles/others/2606291002239275/Photocatalysis-26040151-SM-FC-done.pdf. Figure S1: Regions of ATR-FTIR spectra showing the typical N-H stretching (top) and C-N stretching (bottom) of C_3N_4 prepared from different precursors. Figure S2: The UV-vis diffuse reflectance absorption spectra of C_3N_4 prepared from different precursors. Figure S3: Full XRD patterns (top) and expanded view of the (002) signal (bottom) for exfoliated C_3N_4 materials. Figure S4: UV-vis diffuse reflectance spectra of exfoliated C_3N_4 materials prepared from melamine. Figure S5: XRD pattern of CN-M materials after platinum photodeposition performed by a variation of the general procedure. Figure S6: The UV-vis diffuse reflectance absorption spectra of platinum-loaded graphitic carbon nitride materials.

Author Contributions

L.C.V.-V.: performed the experimental part, drafted the manuscript; A.P.: conceptualized the research, drafted and edited the manuscript; N.B.: optimized synthetic protocols, edited the manuscript; M.G.: edited the manuscript; H.K.: optimized synthetic protocols. All authors have revised and agreed to the published version of the manuscript.

Funding

This work was funded by the NextGenerationEU programme via the Spanish Research Agency and the European Union (funder: MCIN/AEI/10.13039/501100011033; codes: CPP2021-008619, TED2021-129496B-I00) and by the Generalitat de Catalunya, Agència de Gestió d’Ajuts Universitaris i de Recerca via grant number 2021 SGR 00033.

Institutional Review Board Statement

Not applicable.

Informed Consent Statement

Not applicable.

Data Availability Statement

Data will be made available upon request.

Acknowledgments

L.C.V.-V. thanks Universitat Rovira i Virgili (URV) for a predoctoral contract (Martí i Franquès Program, ref. 2021PMF-PIPF-15). H.K. thanks the Erasmus+ KA 107 programme for a placement mobility scholarship.

Conflicts of Interest

The authors declare no conflict of interest.

Use of AI and AI-Assisted Technologies

No AI tools were utilized for this paper.

References

1. Puga, A. (Ed.) *Photocatalytic Hydrogen Production for Sustainable Energy*; Wiley: Weinheim, Germany, 2023.
2. Wang, X.; Maeda, K.; Thomas, A.; et al. A Metal-Free Polymeric Photocatalyst for Hydrogen Production from Water under Visible Light. *Nat. Mater.* **2009**, *8*, 76–80.
3. Wang, X.; Blechert, S.; Antonietti, M. Polymeric Graphitic Carbon Nitride for Heterogeneous Photocatalysis. *ACS Catal.* **2012**, *2*, 1596–1606.
4. Yue, D.; Raj, S.N.M.; Kumar, J.V.; et al. History of Metal Free g-C_3N_4 Photocatalysts for Hydrogen Production: A Comprehensive Review. *Diamond Relat. Mater.* **2024**, *146*, 111228.
5. Prasad, C.; Tang, H.; Liu, Q.; et al. A Latest Overview on Photocatalytic Application of g-C_3N_4 Based Nanostructured Materials for Hydrogen Production. *Int. J. Hydrogen Energy* **2020**, *45*, 337–379.
6. Cao, S.; Low, J.; Yu, J.; et al. Polymeric Photocatalysts Based on Graphitic Carbon Nitride. *Adv. Mater.* **2015**, *27*, 2150–2176.
7. Li, H.; Zhang, Z.; Liu, Y.; et al. Functional Group Effects on the HOMO–LUMO Gap of g-C_3N_4. *Nanomaterials* **2018**, *8*, 589.
8. Cao, S.; Yu, J. g-C_3N_4-Based Photocatalysts for Hydrogen Generation. *J. Phys. Chem. Lett.* **2014**, *5*, 2101–2107.

9. Dong, G.; Zhang, Y.; Pan, Q.; et al. A Fantastic Graphitic Carbon Nitride (g-C_3N_4) Material: Electronic Structure, Photocatalytic and Photoelectronic Properties. *J. Photochem. Photobiol. C* **2014**, *20*, 33–50.
10. Guo, R.-T.; Wang, J.; Bi, Z.-X.; et al. Recent Advances and Perspectives of g–C_3N_4–Based Materials for Photocatalytic Dyes Degradation. *Chemosphere* **2022**, *295*, 133834.
11. Smýkalová, A.; Sokolová, B.; Foniok, K.; et al. Photocatalytic Degradation of Selected Pharmaceuticals Using g-C_3N_4 and TiO_2 Nanomaterials. *Nanomaterials* **2019**, *9*, 1194.
12. Oh, W.-D.; Lok, L.-W.; Veksha, A.; et al. Enhanced Photocatalytic Degradation of Bisphenol A with Ag-Decorated S-Doped g-C_3N_4 under Solar Irradiation: Performance and Mechanistic Studies. *Chem. Eng. J.* **2018**, *333*, 739–749.
13. Sun, S.; Fan, E.; Xu, H.; et al. Enhancement of Photocatalytic Activity of g-C_3N_4 by Hydrochloric Acid Treatment of Melamine. *Nanotechnology* **2019**, *30*, 315601.
14. Zhang, C.; Liu, J.; Huang, X.; et al. Multistage Polymerization Design for g-C_3N_4 Nanosheets with Enhanced Photocatalytic Activity by Modifying the Polymerization Process of Melamine. *ACS Omega* **2019**, *4*, 17148–17159.
15. Wang, Y.; Tan, G.; Dang, M.; et al. Study on Surface Modification of g-C_3N_4 Photocatalyst. *J. Alloys Compd.* **2022**, *908*, 164507.
16. Yan, W.; Yan, L.; Jing, C. Impact of Doped Metals on Urea-Derived g-C_3N_4 for Photocatalytic Degradation of Antibiotics: Structure, Photoactivity and Degradation Mechanisms. *Appl. Catal. B Environ.* **2019**, *244*, 475–485.
17. Yang, C.; Tan, Q.; Li, Q.; et al. 2D/2D Ti_3C_2 MXene/g-C_3N_4 Nanosheets Heterojunction for High Efficient CO_2 Reduction Photocatalyst: Dual Effects of Urea. *Appl. Catal. B Environ.* **2020**, *268*, 118738.
18. Li, Y.; Jin, Z.; Zhang, L.; et al. Controllable Design of Zn-Ni-P on g-C_3N_4 for Efficient Photocatalytic Hydrogen Production. *Chin. J. Catal.* **2019**, *40*, 390–402.
19. Qian, X.-B.; Peng, W.; Huang, J.-H. Fluorescein-Sensitized Au/g-C_3N_4 Nanocomposite for Enhanced Photocatalytic Hydrogen Evolution under Visible Light. *Mater. Res. Bull.* **2018**, *102*, 362–368.
20. Zhang, J.; Chen, Y.; Wang, X. Two-Dimensional Covalent Carbon Nitride Nanosheets: Synthesis, Functionalization, and Applications. *Energy Environ. Sci.* **2015**, *8*, 3092–3108.
21. Zhao, Z.; Sun, Y.; Dong, F. Graphitic Carbon Nitride Based Nanocomposites: A Review. *Nanoscale* **2015**, *7*, 15–37.
22. Fang, L.; Ohfuji, H.; Shinmei, T.; et al. Experimental Study on the Stability of Graphitic C_3N_4 under High Pressure and High Temperature. *Diamond Relat. Mater.* **2011**, *20*, 819–825.
23. Li, Y.; Li, X.; Zhang, H.; et al. Porous Graphitic Carbon Nitride for Solar Photocatalytic Applications. *Nanoscale Horiz.* **2020**, *5*, 765–786.
24. Liu, J.; Wang, H.; Antonietti, M. Graphitic Carbon Nitride "Reloaded": Emerging Applications beyond (Photo)catalysis. *Chem. Soc. Rev.* **2016**, *45*, 2308–2326.
25. Cui, L.; Hou, X.; Du, H.; et al. Facile One-Step "Polymerization-Exfoliation" Route to Crystalline Graphitic Carbon Nitride Nanosheets for Increased Photocatalytic Hydrogen Evolution. *Appl. Surf. Sci.* **2020**, *501*, 144259.
26. Zhang, M.; Yang, Y.; An, X.; et al. Exfoliation Method Matters: The Microstructure-Dependent Photoactivity of g-C_3N_4 Nanosheets for Water Purification. *J. Hazard. Mater.* **2022**, *424*, 127424.
27. Iqbal, A.; Altalhi, K.M.; Samy, B.A.; et al. Photocatalytic H_2 Production over Exfoliated g-C_3N_4 Nanosheets Prepared at Different Treatment Conditions. *Int. J. Hydrogen Energy* **2025**, *127*, 666–677.
28. Puga, A.V. Photocatalytic Production of Hydrogen from Biomass-Derived Feedstocks. *Coord. Chem. Rev.* **2016**, *315*, 1–66.
29. Speltini, A.; Pisanu, A.; Profumo, A.; et al. Rationalization of Hydrogen Production by Bulk g-C_3N_4: An In-Depth Correlation between Physico-Chemical Parameters and Solar Light Photocatalysis. *RSC Adv.* **2018**, *8*, 39421–39431.
30. Zhurenok, A.V.; Vasilchenko, D.B.; Kozlova, E.A. Comprehensive Review on g-C_3N_4-Based Photocatalysts for the Photocatalytic Hydrogen Production under Visible Light. *Int. J. Mol. Sci.* **2023**, *24*, 346.
31. Herrera-Beurnio, M.C.; López-Tenllado, F.J.; Hidalgo-Carrillo, J.; et al. Controlled Photodeposition of Pt onto TiO_2-g-C_3N_4 Systems for Photocatalytic Hydrogen Production. *Catal. Today* **2023**, *413–415*, 113967.
32. Liu, M.; Xia, P.; Zhang, L.; et al. Enhanced Photocatalytic H_2-Production Activity of g-C_3N_4 Nanosheets via Optimal Photodeposition of Pt as Cocatalyst. *ACS Sustain. Chem. Eng.* **2018**, *6*, 10472–10480.
33. Wang, K.; Wang, X.; Pan, H.; et al. *In Situ* Fabrication of CDs/g-C_3N_4 Hybrids with Enhanced Interface Connection via Calcination of the Precursors for Photocatalytic H_2 Evolution. *Int. J. Hydrogen Energy* **2018**, *43*, 91–99.
34. Zhang, Y.; Liu, J.; Wu, G.; et al. Porous Graphitic Carbon Nitride Synthesized via Direct Polymerization of Urea for Efficient Sunlight-Driven Photocatalytic Hydrogen Production. *Nanoscale* **2012**, *4*, 5300–5303.
35. Paul, D.R.; Sharma, R.; Nehra, S.P.; et al. Effect of Calcination Temperature, pH and Catalyst Loading on Photodegradation Efficiency of Urea Derived Graphitic Carbon Nitride towards Methylene Blue Dye Solution. *RSC Adv.* **2019**, *9*, 15381–15391.
36. Saman, F.; Se Ling, C.H.; Ayub, A.; et al. Review on Synthesis and Modification of g-C_3N_4 for Photocatalytic H_2 Production. *Int. J. Hydrogen Energy* **2024**, *77*, 1090–1116.
37. Liu, J.; Zhang, T.; Wang, Z.; et al. Simple Pyrolysis of Urea into Graphitic Carbon Nitride with Recyclable Adsorption and Photocatalytic Activity. *J. Mater. Chem.* **2011**, *21*, 14398–14401.

38. Lan, H.; Li, L.; An, X.; et al. Microstructure of Carbon Nitride Affecting Synergetic Photocatalytic Activity: Hydrogen Bonds vs. Structural Defects. *Appl. Catal. B Environ.* **2017**, *204*, 49–57.
39. Zhou, J.; Xue, J.; Pan, Q.; et al. A Gas Bubble Exfoliation Method to Prepare g-C_3N_4 Nanosheets with Enhanced Photocatalytic Activities. *J. Photochem. Photobiol. A Chem.* **2019**, *372*, 147–155.
40. Al-Azri, Z.H.N.; Chen, W.-T.; Chan, A.; et al. The Roles of Metal Co-Catalysts and Reaction Media in Photocatalytic Hydrogen Production: Performance Evaluation of M/TiO_2 Photocatalysts (M = Pd, Pt, Au) in Different Alcohol-Water Mixtures. *J. Catal.* **2015**, *329*, 355–367.
41. Zhang, N.; Han, C.; Xu, Y.-J.; et al. Near-Field Dielectric Scattering Promotes Optical Absorption by Platinum Nanoparticles. *Nat. Photonics* **2016**, *10*, 473–482.
42. Zhu, B.; Xia, P.; Ho, W.; et al. Isoelectric Point and Adsorption Activity of Porous g-C_3N_4. *Appl. Surf. Sci.* **2015**, *344*, 188–195.
43. Dong, S.; Zeng, Z.; Cai, W.; et al. The Zeta Potentials of g-C_3N_4 Nanoparticles: Effect of Electrolyte, Ionic Strength, pH, and Humic Acid. *J. Nanopart. Res.* **2019**, *21*, 233.
44. Cohen, J.L.; Volpe, D.J.; Abruña, H.D. Electrochemical Determination of Activation Energies for Methanol Oxidation on Polycrystalline Platinum in Acidic and Alkaline Electrolytes. *Phys. Chem. Chem. Phys.* **2007**, *9*, 49–77.
45. Grupi, A.; Minton, A.P. Capillary Viscometer for Fully Automated Measurement of the Concentration and Shear Dependence of the Viscosity of Macromolecular Solutions. *Anal. Chem.* **2012**, *84*, 10732–10736.
46. Kirinčič, S.; Klofutar, C. Viscosity of Aqueous Solutions of Poly(ethylene glycol)s at 298.15 K. *Fluid Phase Equilib.* **1999**, *155*, 311–325.
47. Karimi Estahbanati, M.R.; Feilizadeh, M.; Attar, F.; et al. Current Developments and Future Trends in Photocatalytic Glycerol Valorization: Photocatalyst Development. *Ind. Eng. Chem. Res.* **2020**, *59*, 22330–22352.
48. Lan, L.; Daly, H.; Sung, R.; et al. Mechanistic Study of Glucose Photoreforming over TiO_2-Based Catalysts for H_2 Production. *ACS Catal.* **2023**, *13*, 8574–8587.
49. Sanwald, K.E.; Berto, T.F.; Eisenreich, W.; et al. Overcoming the Rate-Limiting Reaction during Photoreforming of Sugar Aldoses for H_2-Generation. *ACS Catal.* **2017**, *7*, 3236–3244.
50. Edirisooriya, E.M.N.T.; Senanayake, P.S.; Wang, H.B.; et al. Photo-Reforming and Degradation of Waste Plastics under UV and Visible Light for H_2 Production Using Nanocomposite Photocatalysts. *J. Environ. Chem. Eng.* **2023**, *11*, 109580.
51. Roebuck, L.; Daly, H.; Lan, L.; et al. H_2 Production from the Photocatalytic Reforming of Ethylene Glycol: Effect of TiO_2 Crystalline Phase on Photo-Oxidation Mechanism. *J. Catal.* **2025**, *442*, 115876.
52. Lau, V.W.-H.; Yu, V.W.-Z.; Ehrat, F.; et al. Urea-Modified Carbon Nitrides: Enhancing Photocatalytic Hydrogen Evolution by Rational Defect Engineering. *Adv. Energy Mater.* **2017**, *7*, 1602251.
53. Wu, P.; Wang, J.; Zhao, J.; et al. High Alkalinity Boosts Visible Light Driven H_2 Evolution Activity of g-C_3N_4 in Aqueous Methanol. *Chem. Commun.* **2014**, *50*, 15521–15524.
54. Haleem, Y.A.; He, Q.; Liu, D.; et al. Facile Synthesis of Mesoporous Detonation Nanodiamond-Modified Layers of Graphitic Carbon Nitride as Photocatalysts for the Hydrogen Evolution Reaction. *RSC Adv.* **2017**, *7*, 15390–15396.
55. Liang, Y.-F.; Lu, J.-R.; Tian, S.-K.; et al. Pt Nanoclusters Modified Porous g-C_3N_4 Nanosheets to Significantly Enhance Hydrogen Production by Photocatalytic Water Reforming of Methanol. *Chin. J. Chem. Eng.* **2024**, *66*, 40–50.
56. Herrera-Beurnio, M.C.; López-Tenllado, F.J.; Hidalgo-Carrillo, J.; et al. Glycerol Photoreforming for Photocatalytic Hydrogen Production on Binary and Ternary Pt-g-C_3N_4-TiO_2 Systems: A Comparative Study. *Catal. Today* **2024**, *430*, 114548.
57. Kurenkova, A.Y.; Kharina, S.N.; Aydakov, E.E.; et al. Hydrogen Production from Aqueous Glucose Solutions over g-C_3N_4/Pt/TiO_2 Photocatalysts. *Kinet. Catal.* **2024**, *65*, 703–709.